Computationally Efficient Millimeter-Wave Scattering Models: A Multiple-Scattering Model

Adrián Lahuerta-Lavieja, Martin Johansson, Christina Larsson,
Ulf Gustavsson, and Guy A. E. Vandenbosch

Abstract: Backscattering is an essential phenomenon in millimeter-wave (mm-wave) propagation. Accordingly, computationally efficient models characterizing this process are now available in the literature. However, these models are restricted to single-surface contributions. In this paper, we propose a multiple-scattering model for calculating backscattered fields due to consecutive interactions with several rectangular surfaces. In addition, the model is later extended to capture single-scattering blockage between backscattering events. The model is implemented using a Fresnel-integral-based method and validated by means of electromagnetic (EM) simulations and measurements. Furthermore, insight on the effects of the model parameters—number of surfaces, frequency, surface size, surface height-to-width ratio, surface displacement, and antenna-to-surface and surface-to-surface distances—is provided. Due to its computational efficiency, the proposed model can be suitable for system and link-level simulations of wireless systems, particularly when Monte Carlo simulations are applied.

Computationally Efficient Millimeter-Wave Scattering Models: A Multiple-Scattering Model

Adrián Lahuerta-Lavieja, Martin Johansson, *Senior Member, IEEE*, Christina Larsson, Ulf Gustavsson, and Guy A. E. Vandenbosch, *Fellow, IEEE*

Abstract—Backscattering by objects is a relevant phenomenon in millimeter-wave (mm-wave) propagation. Accordingly, computationally efficient models characterizing this process are now available in the literature. However, these models are restricted to single-surface contributions. In this paper, we propose a multiple-scattering model for calculating backscattered fields due to consecutive interactions with several smooth electrically-large rectangular surfaces. The model is fundamentally based on the cascading of single-scattering events. In addition, the model is later extended to capture single-scattering blockage between backscattering events. The model is implemented using a Fresnel-integral-based method and validated by means of electromagnetic (EM) simulations and measurements. Furthermore, insight on the effects of the model parameters—number of surfaces, frequency, surface size, surface height-to-width ratio, surface displacement, and antenna-to-surface and surface-to-surface distances—is provided. Due to its computational efficiency, the proposed model can be suitable for system- and link-level simulations of wireless systems, particularly when Monte Carlo simulations are applied.

Index Terms—5G mobile communication, channel model, computational complexity, electromagnetic scattering, Fresnel integral, millimeter wave propagation.

I. INTRODUCTION

MILLIMETER-WAVE (mm-wave) frequency bands are expected to help us achieve the data rates envisioned for the fifth-generation cellular mobile communications (5G) [1] and beyond. For this reason, mm-wave research has become a topic of interest over the last decade. Besides, the use of high-gain narrow-beam antenna systems like massive multiple-input-multiple-output (MIMO) in 5G networks will allow drastically increased radiated energy efficiency [2].

However, mm-wave high-gain antenna systems are highly sensitive to blockage of the line-of-sight (LoS) component between base station and user antennas [3]. Hence, reliable

blockage modeling becomes of great importance and a number of accessible blockage models, such as the METIS [4, Sec. C.1.4] and mmMAGIC [5, Sec. 4.6.3] models have been proposed and tested over the last years [6]. These screen-oriented models are, explicitly or implicitly, based on evaluating phase differences due to excess path lengths of rays passing around the edges of a rectangular surface or screen. The major advantage of these models is their size-independence with respect to computational complexity, and thus they are dramatically faster to evaluate than more detailed electromagnetic (EM) models when surfaces become large in terms of wavelengths.

Similarly to blockage, backscattering is another propagation mechanism whose importance grows at mm-wave frequencies, where traditionally small objects seem to generate more evident and specular-like contributions, probably due to their larger size compared to the wavelength [7]. Yet, computationally efficient alternatives for calculating backscattering phenomena are scarcer. For example, only a farfield backscattering model based on the radar cross section (RCS) of a sphere was proposed by METIS [4, Sec. C.1.5].

Inspired by the simple, efficient, screen-oriented blockage models referred to above, a single-scattering model for calculating backscattered fields from smooth electrically-large rectangular surfaces based on evaluating excess path length phase differences was introduced in [8]. Of the models studied in [8], the 3D Fresnel model was shown to be the most accurate both in magnitude and phase when tested for different surface orientation, surface position, antenna pointing, and distance to the scatterer. Furthermore, the 3D Fresnel model asymptotically approaches the RCS solution for large distances [8, Fig. 7(a)], [9, Fig. 1]. Lastly, performance of this model at different mm-wave frequencies and for single-scattering from multiple surfaces was demonstrated in [10].

One alternative to screen-oriented models is the uniform geometrical theory of diffraction (UTD), which is an edge-based high-frequency model for calculating scattering from an object [11]. Since its conception, UTD has been further developed to handle different types of diffraction problems, see, for example, [12], [13]. Another alternative is the very simple, and computationally-efficient, recursive model introduced by Berg [14], which models macro-scale diffraction behavior in urban scenarios. Both UTD, which offers a general diffraction solution, and the Berg model, which offers a model restricted to specific use cases, are edge-based models. Our focus is instead on screen-oriented models, as in [4] and [5].

A computationally-efficient multiple-scattering model that

could maintain the processing gains achieved in [8] is of interest. Similarly to the single-scattering model, this simplified multiple-scattering model would be well suited for simulations of indoor or outdoor scenarios where fast, efficient calculations are of the essence for electrically-large surfaces, for example, in system- and link-level simulations of wireless systems, particularly when Monte Carlo simulations are applied. Also, for ray-tracing (RT) modeling, where the number of potential paths can grow exponentially for diffuse and diffraction-like ray interactions, means for early pruning is of the essence. Hence, integrated approximate, but computationally efficient, path loss models could then be used, for example, to prune non-contributing candidate paths on-the-fly. The models can be applied to surfaces that either represent an actual scenario or are generated based on distributions for position, size, etc. Furthermore, the model could be a good match to be used with RT (path finding, in propagation applications) and, for planar surfaces, offers a way to support heterogeneous material characteristics, i.e, a surface can be subdivided into multiple surfaces with distinct homogeneous material characteristics.

In this paper, we propose a multiple-scattering model for calculating scattered fields from consecutive interactions on multiple smooth electrically-large rectangular surfaces. The multiple-scattering model is fundamentally based on the cascading of single-scattering events [8]. The model supports both consecutive backscattering from an arbitrary number of surfaces and single-scattering blockage between backscattering events. The results and validation presented in this paper are based on a 3D Fresnel model but could also be implemented using any other of the models evaluated in [8].

The remainder of the paper is structured as follows. Section II introduces the multiple-scattering model, which is validated by means of EM simulations and measurements in Sections III and IV, respectively. Finally, Section V concludes this paper.

II. MULTIPLE-SCATTERING MODEL

A signal radiated from a transmit (Tx) antenna may interact with an object before impinging on a receive (Rx) antenna. This is what we refer to as single-scattering, and there may be one or more of this type of interaction. The signal may also impinge on the Rx antenna after consecutive interactions on multiple objects. The latter is what we here consider as multiple scattering.

Using image theory, a signal reflected by an infinite plane surface may alternatively be modeled as a signal transmitted from an image source mirrored on the plane of the surface. Similarly, a signal reflected by multiple infinite plane surfaces may be modeled as a signal transmitted from an image source consecutively and orderly mirrored on the planes of the surfaces [15]. When one of those infinite planes is replaced by a finite surface, the resulting signal after the same reflection process described above may be calculated using the single-scattering model [8]. When we go a step further and a second infinite plane is also replaced by a finite surface, the situation becomes a bit different. For simplified modeling purposes, we assume the first finite surface to be infinite when modeling the backscattering from the second finite surface. The combination

of the two single-surface contributions can then be used as an approximation to the actual signal scattered in the two finite surfaces.

Hence, we propose the modeling of EM components arising from consecutive interactions in multiple finite surfaces as independent single-scattering events. For that, the single-scattering equation [8, eq. (4)] may be used as baseline. Then, the channel contribution of the mth multiple-scattered component h_m is written as

$$h_m = g_{\text{Tx}}\left(\theta'_j, \phi'_j\right) \Gamma^{\text{M}}_m g_{\text{Rx}}\left(\theta''_k, \phi''_k\right) \frac{\lambda}{4\pi} \frac{e^{-jkd_m}}{d_m} \tag{1}$$

where Γ^{M}_m is the multiple-scattering coefficient corresponding to the mth multiple interaction ("M" signifying multiple), g_{Tx} and g_{Rx} are the Tx and Rx antenna gains ($g_{\text{Tx}} = \sqrt{G_{\text{Tx}}}$ and $g_{\text{Rx}} = \sqrt{G_{\text{Rx}}}$ where G_{Tx} and G_{Rx} are the linear power gains), respectively, θ'_j and ϕ'_j are elevation and azimuth angles, respectively, towards the *antenna gain reference point* in the first scattering surface j of the multiple interaction m in the Tx local coordinate system, and θ''_k and ϕ''_k are elevation and azimuth angles, respectively, towards the *antenna gain reference point* in the last scattering surface k of the multiple interaction m in the Rx local coordinate system, and $k = 2\pi/\lambda$ is the wavenumber, with λ being the wavelength. The factor $\lambda/4\pi$ is included to take into account the power density of the transmitted field and the effective area of the Rx antenna. Furthermore, d_m is the distance from the Tx antenna to the Rx antenna via the multiple specular reflection points P^{M}_0 in the planes defined by the scatterers considered in the mth interaction. For example, $d_m = d_{\text{A}} + d_{\text{B}} + d_{\text{C}}$ for the interaction Tx-Surface j-Surface k-Rx drawn in Fig. 1.

The *antenna gain reference point* is the point used to compute antenna gains in the single-scattering model [8]. This point is P^{M}_0, if contained within the ith scattering surface, or the point in the scattering surface closest to P^{M}_0. Differently to the single-scattering model, where only one antenna gain reference point is used, two antenna gain reference points are used in the multiple-scattering model: one in the first scattering surface of the multiple interaction m to compute Tx antenna gain and one in the last scattering surface of the multiple interaction m to compute Rx antenna gain. For example, the antenna gain reference points in surfaces j and k for the sequence of surfaces (j, k) depicted in Fig. 1 are $P_{\text{W}1_j}$ and P_{0_k}, respectively. Moreover, $\text{P}_{\text{W}1_j}$ and $\text{P}_{\text{W}2_j}$ denote the points on the line defined by the closest and furthest edges to P_{0_j} in the width dimension of surface j, respectively, as indicated in Fig. 1.

Similarly to [8, eq. (4)], the *ray optical continuation* at high frequencies has been applied in (1): the divergence factor governs the amplitude variation of the geometrical optics field along the ray path [16]. Hence, we have that the amplitude attenuation of the field scattered by multiple surfaces is the sum of distances between multiple specular reflection points rather than their product. This approximation is strictly valid only for electrically-large planar surfaces with all specular reflection points falling within the corresponding surfaces. The proposed model is in fact intended to be used for smooth electrically-large rectangular surfaces, which is a reasonable
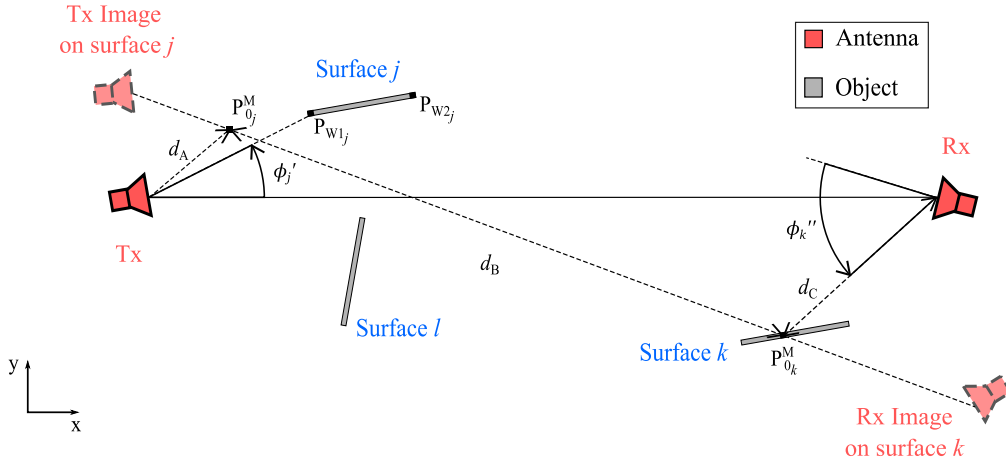
Fig. 1. Top projection of a scenario containing multiple surfaces. Essential points and angles have been drawn for a multiple interaction going from the Tx to the Rx antenna via one permitted sequence of surfaces, (j, k). Furthermore, mirror images of the Tx and Rx antennas in surfaces j and k, respectively, have been drawn for readability.

assumption for many everyday objects at mm-waves and beyond: building walls, billboards, vehicles, etc. [8].

The multiple-scattering coefficient corresponding to the mth multiple interaction Γ_m^{M} is calculated as the product of single-scattering coefficients Γ_{a_n} calculated for each surface a_n in the multiple interaction. This is

$$\Gamma_m^{\mathrm{M}} = \prod_{(a_n)_{n \in \mathbb{N}}} \Gamma_{a_n} \qquad (2)$$

where $(a_n)_{n \in \mathbb{N}}$ is any sequence from the set S, which contains all surfaces in the scenario, in which non-consecutive repetition of elements is allowed, that is, a surface cannot interact directly with itself but is allowed to interact with others for a finite number of times. Furthermore, the sequence order must be such that all surfaces are backscattering when we trace a path from the Tx to the Rx antenna through the sequence of surfaces $(a_n)_{n \in \mathbb{N}}$ and there is LoS between antennas and surfaces in the path. For instance, for the scenario containing surfaces j, k, and l in Fig. 1, an example of a permitted sequence is (j, k) or, equivalently, $a_1 = j$ and $a_2 = k$, whereas an example of a forbidden sequence is (j, l, k).

Essentially, $\Gamma_{a_n} = \Gamma_{a_n}^{\mathrm{F}} \cdot \Gamma_{a_n}^{\mathrm{G}}$ models the effect of the a_nth surface in the scattering process: the Fresnel reflection coefficient $\Gamma_{a_n}^{\mathrm{F}}$ [17, pp. 179-180] represents the material properties of the surface while the geometrical coefficient $\Gamma_{a_n}^{\mathrm{G}}$ captures the effect of its geometry, that is, its position and orientation, and is calculated using any of the backscattering models available in the literature and reproduced here for completeness. Γ_i^{G} is given by $\Gamma_i^{\mathrm{G}} = \Gamma_i^{\mathrm{W}} \cdot \Gamma_i^{\mathrm{H}}$, where Γ_i^{W} and Γ_i^{H} are independent scattering coefficients calculated in the width and height dimensions of the scattering surface, respectively [8]. Γ^{W} is calculated as [8, eq. (11)]

$$\Gamma^{\mathrm{W}} = \begin{cases} K_m \big[f_m(\nu_{\mathrm{W2}}) + f_m(\nu_{\mathrm{W1}}) \big], & \mathrm{P}_0^{\mathrm{M}} \text{ is between } \mathrm{P}_{\mathrm{W1}} \text{ and } \mathrm{P}_{\mathrm{W2}} \\ K_m \big[f_m(\nu_{\mathrm{W2}}) - f_m(\nu_{\mathrm{W1}}) \big], & \text{otherwise} \end{cases} \qquad (3)$$

where f_m denotes the function among the models as indicated in Table I, ν_{W1} and ν_{W2} are the Fresnel-Kirchhoff diffraction parameters due to the excess path length from the Tx antenna

TABLE I
MODEL FUNCTIONS [9, TABLE I]

Model (m)	$f_m(\cdot)$	K_m
3D Fresnel	[8, eq. (7)]	$(1+j)/2$
erf	[8, eq. (10)]	$1/2$
M-METIS	[4, eq. (C-8)]	1
M-ITU SE	[18, eq. (75)]]	1
M-ITU Fresnel	[18, eq. (72)–(73)]	$(1+j)/2$

to the Rx antenna via P_{W1} and P_{W2}, respectively, and K_m is a complex normalization constant (see Table I). The same reasoning applies along the height dimension for calculating Γ^{H} (see [8] for details).

Relatedly, in the far-field limit, that is, when a surface is small relative to the distance between surface and antennas and thus the excess path length tends to zero, the magnitude of the Fresnel-integral-based single-scattering geometrical coefficient $\Gamma_{a_n}^{\mathrm{G}}$ is directly proportional to the area of the scattering surface and inversely proportional to the total distance between the antennas via the surface. Hence, the Fresnel models reduce to the RCS solution (assuming surface size much greater than λ and observation at normal direction). Essentially, this makes the Fresnel models applicable not only in the near-field but also in the far-field limit as illustrated for large distances in [9, Fig. 1].

EM image theory [15] has generally been used in RT algorithms [19], [20] to determine virtual antenna positions due to reflections in surfaces. The same principle was followed in [8] to calculate the single-scattering model. In the present multiple-scattering model, the geometrical coefficient of the a_nth surface $\Gamma_{a_n}^{\mathrm{G}}$ is calculated by consecutively and orderly— according to the order defined by the sequence $(a_n)_{n \in \mathbb{N}}$— mirroring the Tx and Rx antennas in all the previous and posterior surfaces, respectively, to the target surface. In the case of the Tx antenna, it is also mirrored one last time in the a_nth surface to compute the method as described in (3) and in [8]. That is, once virtual positions of the antennas are

obtained, extra path lengths through the a_nth surface edges and the Fresnel-Kirchhoff diffraction parameters ν_{W1} and ν_{W2} are computed and applied in (3) for calculating the single-surface geometrical coefficient $\Gamma^G_{a_n}$. Hence, for each surface a_n, all the remaining surfaces considered in the sequence $(a_n)_{n \in \mathbb{N}}$ defining the multiple interaction are only used for obtaining the virtual antenna positions. Once the described procedure is applied to all surfaces in $(a_n)_{n \in \mathbb{N}}$, Γ^M_m is calculated as a product of single-surface geometrical coefficients, see (2).

Finally, the model is scalar, and hence does not include effects related to the polarization state of the incident field, and reciprocal. Note that, in the limiting case of one surface interaction, the multiple-scattering model reduces to the single-scattering model proposed in [8].

A. Extension to Single-Scattering Blockage

When a surface is blocking the traced path from the Tx to the Rx antenna through the sequence of surfaces $(a_n)_{n \in \mathbb{N}}$, (2) then modifies to

$$\Gamma^M_m = \prod_{(a_n)_{n \in \mathbb{N}}} \Gamma_{a_n} \Gamma^B_{a_n} \qquad (4)$$

where the single-scattering blockage coefficient $\Gamma^B_{a_n}$ is defined in [21, Eq. (2)] for the blockage situation, that is, $\Gamma^B_{a_n} = \left(1 - \Gamma^G_i\right)$. Essentially, Γ^G_i captures the ith surface blockage effect in the incident field on the a_nth surface and is also calculated applying (3) for the same Tx and Rx antenna virtual positions as used for calculating the corresponding Γ_{a_n}, without the last mirroring of the Tx antenna on the a_nth surface.

A special case is when, after backscattering on the last surface of the sequence $(a_n)_{n \in \mathbb{N}}$, the field incident on the Rx antenna is blocked by a surface. In this case, $\Gamma^B_{a_n}$ modifies to $\Gamma^B_{a_n} = \left(1 - \Gamma^G_i\right)\left(1 - \Gamma^{G'}_j\right)$, where $\Gamma^{G'}_j$ captures the jth surface blockage effect in the field incident on the Rx antenna after backscattering on the last surface in $(a_n)_{n \in \mathbb{N}}$. Differently to Γ^G_i, $\Gamma^{G'}_j$ is calculated including one last mirroring of the Tx antenna on the a_nth surface. Different subscripts have been used in Γ^G_i and $\Gamma^{G'}_j$ for generality, but $i = j$ is possible.

$\Gamma^B_{a_n}$ is always a single-scattering coefficient: when multiple surfaces are blocking the field incident on a surface, we follow a maximum criterion. However, for the calculation of blockage loss by multiple surfaces, a Walfisch–Bertoni-based model [6, eq. (16)] may be considered.

Note that (4) follows the same principle followed in (2): the multiple-scattering coefficient Γ^M_m is the product of single-scattering coefficients. Finally, in the absence of blockage, $\Gamma^G_i = 0 \; \forall i \Rightarrow \Gamma^B_{a_n} = 1$, and (4) simply becomes (2).

III. SIMULATION RESULTS

In order to demonstrate the validity of the multiple-scattering model, a performance comparison against more complete simulation models is presented in this section. Physical optics (PO) will be used as the reference model [8]. Firstly, we investigate the model performance using parameter settings mimicking indoor scenarios, that is, relatively short distances

between surfaces and small surface sizes. Secondly, we study the model behavior using typical outdoor scenario settings, that is, longer distances and large surface sizes.

The main carrier frequency used in the simulations is 28 GHz and all scatterers are assumed to be perfect electric conductors (PEC), that is, $\Gamma^F = -1$. Furthermore, the vertically-polarized, that is, z-polarized, Tx and Rx antennas used in the simulations are models of the 21-dBi (Schwarzbeck 9170) and 15-dBi (Narda V637) standard gain horns used in [22], respectively, scaled with the wavelength to have the same radiation properties at all frequencies. The plots in this section show magnitude or phase of (1) assuming unit transmit power, that is, 0 dB. Also, blue-colored numbers are used to distinguish surfaces and surface order in the figure drawings. Lastly, note that the remainder of the paper only includes model results in terms of the 3D Fresnel model, the best performing model among the models evaluated in [8], [21].

The computational complexity of the PO and 3D Fresnel models for single-surface scattering is $\mathcal{O}(N)$ and $\mathcal{O}(1)$, respectively, where N denotes the number of unknowns [8, Table II]. This translated into the 3D Fresnel model providing more than two orders of magnitude faster computation speed than PO, in spite of the Fresnel model being implemented in MAT-LAB. For multiple scattering, the computational complexity of the PO model becomes $\mathcal{O}(N^n)$, where n is the number of surface interactions, while the 3D Fresnel model complexity remains as $\mathcal{O}(1)$. Hence, for the presented multiple-scattering model, the reduction in computational time is even greater in relative terms than for single scattering.

A. Surface Size and Number of Surfaces

To illustrate the performance of the multiple-scattering model in indoor scenario ranges, one, two, and three surfaces have been included in scenarios A, B, and C, respectively, see Fig. 2. In scenario A, one surface is placed with its normal vector creating an angle of 45 degrees with the line drawn from Tx to surface 1. Moreover, the Tx and Rx antennas are pointing toward the surface 1 centroid, see Fig. 2(a). Similarly, in scenario B, surfaces 1 and 2 are placed with their normal vectors creating an angle of 45 degrees with the lines drawn from Tx to surface 1 and from Rx to surface 2, respectively. Furthermore, the Tx and Rx antennas are pointed toward the centroids of surfaces 1 and 2, respectively, see Fig. 2(b). Finally, in scenario C, surface 1 is placed with its normal vector creating an angle of 45 degrees with the line drawn from Tx to surface 1, surface 2 is placed with its normal vector parallel to the line drawn from Tx to surface 2, and surface 3 is placed with its normal vector creating an angle of 45 degrees with the line drawn from Rx to surface 3. Finally, the Tx and Rx antennas are pointed toward the centroids of surfaces 1 and 3, respectively, see Fig. 2(c).

The three scenarios have been designed such that the strongest contribution at the Rx antenna is related to the propagation from Tx to the Rx antenna via the surfaces in numerical order. That is, from Tx antenna via surface 1 to Rx antenna in scenario A, from Tx antenna via surfaces 1 and 2 to Rx antenna in scenario B, and from Tx antenna via surfaces
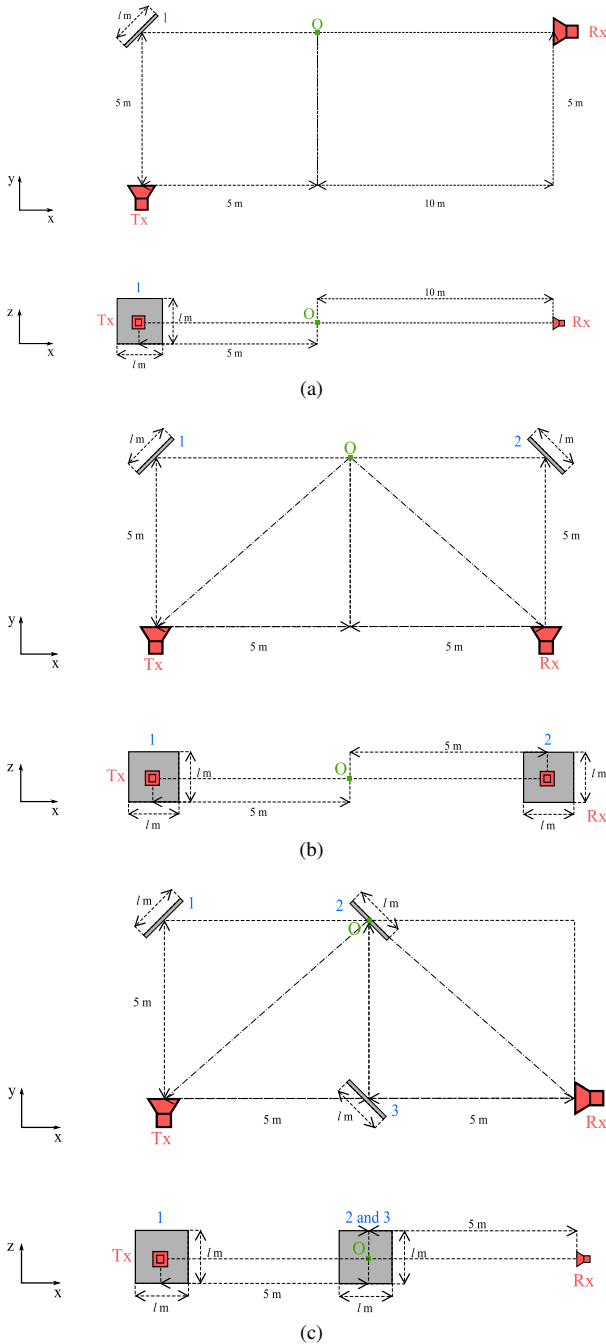
Fig. 2. (a) Scenarios A, (b) B, and (c) C: Test-cases with one, two and three reflecting surfaces, respectively. (a), (b), and (c) show the top and side projections of each scenario.

Fig. 3. Scenarios A, B, and C (a) magnitude and (b) phase results for different surface dimensions.

1, 2, and 3 to Rx antenna in scenario C. In addition, all surface centroids are collocated with the specular reflection points in the respective surfaces, providing the strongest scattering possible according to the Fresnel integrals formulation in (3). Moreover, the distances from the antennas to the surfaces and from surface to surface have been chosen such that the total path length is 20 meters in all three scenarios.

The surfaces in the scenarios are square rectangles whose side length, denoted by l, is varied between 0.1 and 2.5 meters, that is, between 10 and 230λ approximately, which shows the large electrical size of the problem being solved. These sizes could represent indoor objects such as whiteboards, energy-efficient glass, monitors, etc. Figs. 3(a) and 3(b) include results of the three scenarios along with the "free space" Tx-to-Rx results at a distance equal to the total path length for the path from Tx to Rx antenna via the surface centroids, that is, 20 meters. In addition, note that in the scenarios containing an even number of surfaces, that is, scenario B and free space, an extra 180-degree phase shift has been added to align the results and facilitate the visualization and comparison of the phase results ($\Gamma^F = -1$ for each surface). Finally, also note that the figures only show the results of the component travelling from the Tx antenna to the Rx antenna via the surfaces in numerical order, both for the 3D Fresnel model and PO. Nevertheless, the field produced by any other surface sequence can be computed following the same principles, provided that it fulfills the model explained in (2), and proper signal strength for each sequence will be obtained.

Figs. 3(a) and 3(b) show good agreement in magnitude and phase, respectively, of the 3D Fresnel model with the PO reference when applying the multiple-scattering model. It is observed that, as expected, the results for all scenarios tend to the free space result as the surface size increases. Besides, it is also noted that the 3D Fresnel magnitude results deviate from PO results in the three-surface case when the surfaces have an approximate side length of 0.4 m, whereas good performance in phase is maintained. The observed error is a consequence of

TABLE II
PERFORMANCE OF THE PROPOSED MODEL WITH RESPECT TO PO RESULTS

| | | Interval of l | |
| | | [0.1, 2.5] m | [1, 2.5] m |
Scenario	# Surfaces	NMSE (dB)	NMSE (dB)
A	1	-25.7	-24.0
B	2	-20.8	-20.9
C	3	-10.0	-19.3

the discreteness of our model. That is, only using four points on the surface for calculating the surface contribution, as opposed to current-source models, such as PO, that use a number of points on the surface which is proportional to its electrical size. When our discrete approximation is consecutively applied to a number of surfaces, certain combinations of parameter settings—frequency, antenna-to-surface and surface-to-surface distances, surface size, and surface alignment—may result in the proposed model showing larger disagreement with the reference model, as seen in Fig. 3(a).

In order to get a quantitative performance assessment of the multiple-scattering model, the normalized mean square error (NMSE) of scenarios A, B, and C is shown in Table II for two different intervals of l. The NMSE is calculated as [23]

$$\text{NMSE} = 10 \log_{10} \left(\frac{\sum_n |x_n - \hat{x}_n|^2}{\sum_n |x_n|^2} \right) \qquad (5)$$

where x denotes the complex reference signal, that is, the PO model, and $\hat{x}$ denotes the complex estimated signal, that is, the proposed model. Table II shows that, for the interval of l used in the Figs. 3(a) and 3(b), the total NMSE of the three-surface scenario is larger—yet acceptable—than for its one- and two-surface counterparts. As previously mentioned, this is mainly due to a larger error at a specific settings combination where the scattering is maximum. However, if we reduce the interval of l to $[1, 2.5]$ m, the resulting NMSE of scenario C is comparable to the corresponding metric of scenarios A and B, see Table II.

In the interest of illustrating how different scenario settings play a role in the observed model performance, a few tests are studied in the following. This will be done by modifying, one at a time, individual parameter settings used in scenarios B and C, the two- and three-surface cases, respectively. We use a normalized square error (NSE) metric

$$\text{NSE} = 10 \log_{10} \left(\frac{|x_n - \hat{x}_n|^2}{|x_n|^2} \right) \qquad (6)$$

to perform point-to-point comparisons in the following, where x again denotes the complex reference signal, that is, PO, and $\hat{x}$ is the complex estimated signal, that is, the proposed model.

B. Surface Size and Frequency

First, we study the model performance over frequency and surface size. A frequency sweep from 20 to 40 GHz in 2-GHz steps is presented in Fig. 4. Specifically, Figs. 4(a) and 4(b) show that the 3D Fresnel model properly captures
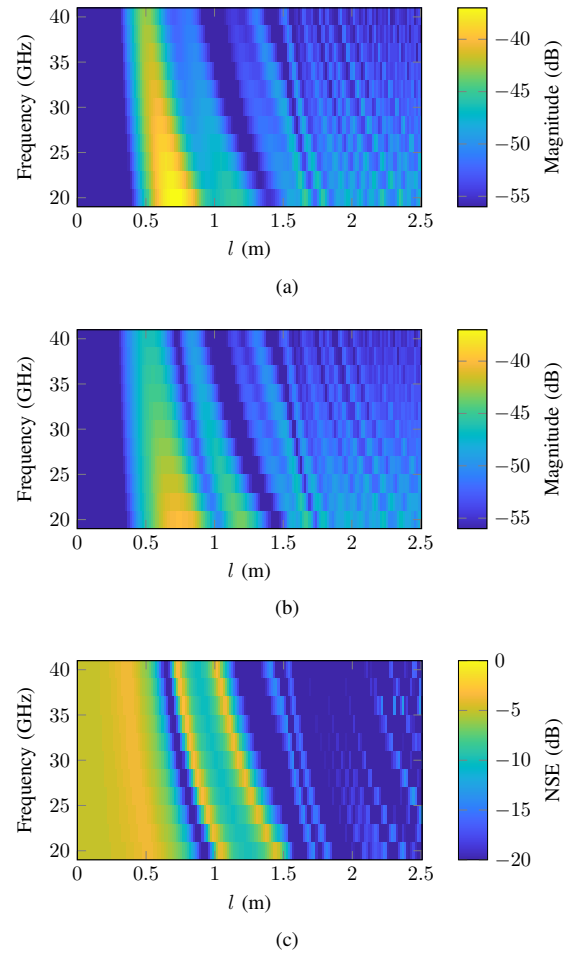

(a)

(b)

(c)

Fig. 4. Scenario C (a) 3D Fresnel and (b) PO magnitude results, and (c) NSE as a function of frequency and surface side length.
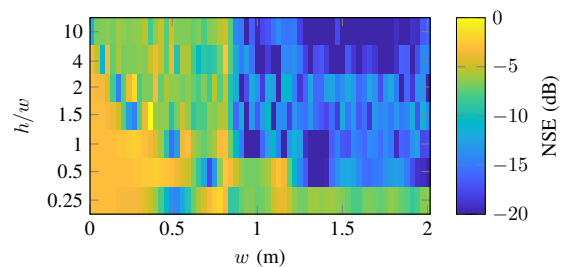

Fig. 5. Scenario C NSE as a function of height to width ratio and surface width dimension.

the PO reference behavior as a function of frequency and l. Fig. 4(c) presents the NSE in dB between the 3D Fresnel and the PO models. Again, we observe that the error decreases as the electrical size of the surface increases. This is again in line with some of the approximations made in the model formulation being strictly valid for electrically-large surfaces; for example, according to Fig. 4(c), larger than 110 and 150λ for 20 and 40 GHz, respectively.

C. Surface Size and Height-to-Width Ratio

Second, we investigate the model performance for non-square rectangles. In this way, we produce larger differences in the extra path length among the horizontal and vertical edges of the surfaces. Fig. 5 presents NSE in dB for different height to width ratios, where h and w denote the height (along the z-axis) and width (in the xy-plane) dimensions of the surface, respectively. Ratios increase from 0.25 to 10 by, roughly, a factor 2 except for ratio $h/w = 1.5$. Note that ratio $h/w = 1$ corresponds to scenario C presented in Fig. 2(c). Again, we observe that the error decreases as the electrical size of the surface increases.

D. Surface Displacement

Third, we explore the effect of surface displacement in scenario B, the two-surface scenario. As in the other scenarios, the surface placement in scenario B was designed for obtaining maximum scattered power in the component travelling from the Tx to the Rx antenna via the surfaces in numerical order. This was achieved by collocating the surface centroids and the specular reflection points in the planes defined by each surface. In the following test, z-axis displacements are performed for fixed-size squared surfaces with $l = 0.4$m with the goal of being in the highest scattered power regime, see Fig. 3(a). Moreover, the displacements range from 0 meters, where the surface centroid is collocated with the specular reflection point in the plane defined by the surface, to 0.5 meters, where the surfaces are far away from the specular reflection points. Furthermore, only positive surface 2 displacements are considered due to symmetry. Note that surface 1 and 2 displacements of zero meters coincide with scenario B presented in Fig. 2(b).

Figs. 6(a) and 6(b) show magnitude results of the 3D Fresnel and PO models, respectively, as a function of surface 1 and 2 displacements along the z-axis, where rapid power decays are observed as surface misalignment increases. Furthermore, as expected, positive and negative displacements of surface 1 produce identical 3D Fresnel results for a given displacement of surface 2, whereas the PO reference shows dependence to the relative displacements of the surfaces, that is, the surfaces moving closer together or further apart. However, Fig. 6(c) shows good agreement between the two models when high scattered power levels are obtained.

E. Surface Size and Distance

Finally, we test our model as a function of antenna-to-surface and surface-to-surface distances. In our study, we set these two distances to be identical just like in scenario C, see Fig. 2(c). In addition, we introduce large-sized scattering surfaces—which are completely prohibitive in terms of PO or full-wave models simulation time—and large distances. That is, potential outdoor scenario settings, where different sizes could represent common street objects such as billboards or vehicles. Fig. 7 shows 3D Fresnel results for different distances between antennas and surfaces as a function of the surface width dimension w. These antenna-to-surface and surface-to-surface distances are denoted as $d_{1/4}$ to symbolize that the
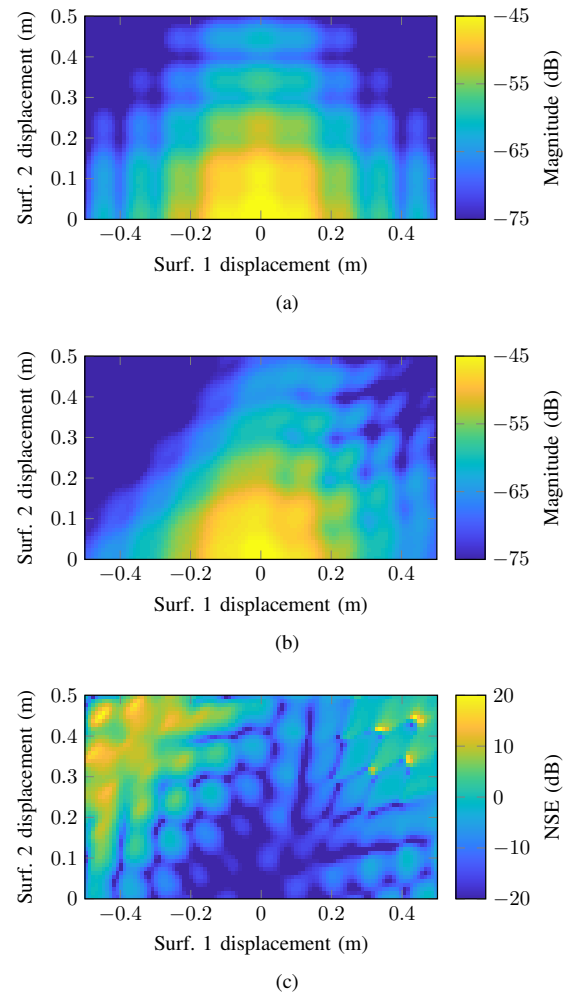

Fig. 6. Scenario B (a) 3D Fresnel and (b) PO magnitude results, and (c) NSE as a function of surface 1 and 2 displacements along the z-axis.

legend integers in Fig. 7 represent one quarter of the total path length of the component travelling from Tx to surface 1, then to surface 2, then to surface 3, and finally to the Rx antenna. Hence, an antenna-to-surface and surface-to-surface distance $d_{1/4}$ represents a total path length of four times $d_{1/4}$. In our study, $d_{1/4}$ takes four different values between 10 and 100 meters with scatterer width dimension ranging from 0 to 10 meters or, equivalently, from 0 to 934λ. Besides, a $h/w = 0.25$ is used to compute 3D Fresnel results in Fig. 7, as an example ratio which could represent billboard or vehicle dimensions. Note that $d_{1/4} = 5$ m in scenario C, see Fig. 2(c). Each $d_{1/4}$ trace is plotted together with the corresponding free space signal at $4 \cdot d_{1/4}$, the total path length of the multiple-scattered contribution. Figs. 7(a) and 7(b) show an increasing variability in magnitude and phase as $d_{1/4}$ grows. This is explained by the fact that, at larger distances, the extra path length through the surface edges becomes smaller relative to the total path length from antenna to antenna via the specular reflection points. Furthermore, the observed fast and small ripples in Fig. 7 results are a consequence of the different rate change of the Fresnel integrals due to the width and height dimensions. The results provided in Fig. 7 can efficiently be obtained by
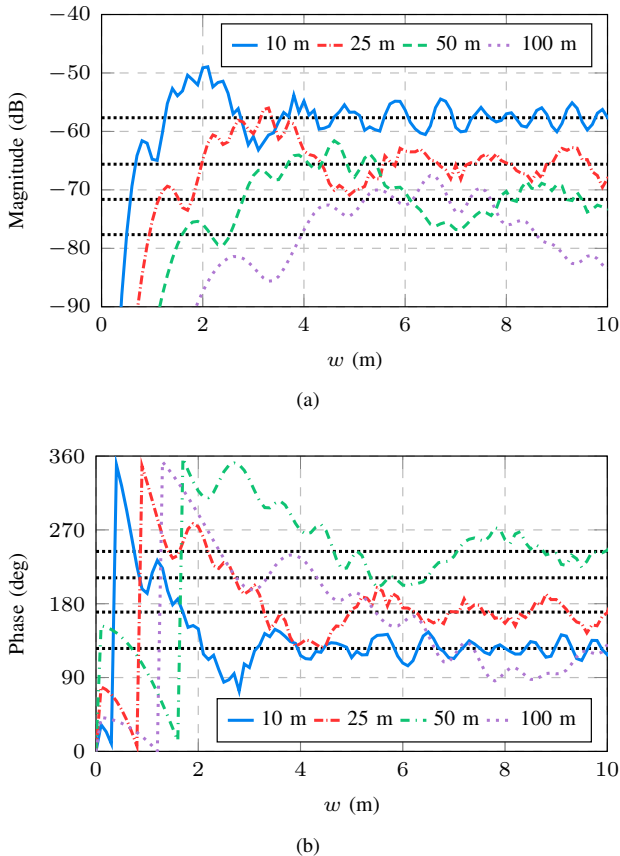
(a)

(b)

Fig. 7. Scenario C 3D Fresnel magnitude results for different antenna-to-surface and surface-to-surface distances $d_{1/4}$ as a function of the scatterer width dimension. Each $d_{1/4}$ trace is plotted together with the corresponding free space signal at $4 \cdot d_{1/4}$ (dotted black).

using the proposed multiple-scattering model despite the large electrical size of the objects.

F. Backscattering and Blockage

Scenario D shows an example of multiple-scattering where the illumination and scattering from a surface is blocked by another surface. For this scenario, two $1{\times}1$-meter parallel surfaces are considered, see Fig. 8(a). Surface 1 is located closer to the line between the Tx and Rx antennas and moved parallel to the *x*-axis whereas surface 2 is static and located further away from the line between the antennas. The antennas are pointed toward surface 2 centroid, which is also the specular reflection point on surface 2.

The scenario is designed such that surface 1 blocks to different degrees the illumination of surface 2 during surface 1 movement. Essentially, surface 1 barely influences the received field at the beginning of its movement interval; blocks the illumination of surface 2 near the middle of the interval; and lastly adds specular reflection at the end of the interval.

Figs. 8(b) and 8(c) show scenario D magnitude and phase results, respectively, considering up to second-order contributions. The contribution from surface 2 ("Surf. 2") represents the superposition of two components, the backscattering of the unblocked and blocked fields, the latter due to the presence

of surface 1. Furthermore, "Total" represents the addition of surface 1 contribution ("Surf. 1"), "Surf. 2", and the direct ("LoS") component, all calculated based on the 3D Fresnel model. In addition, for the sake of readability of Fig. 8(c), Surf. 1 phase results are not shown for the $x = [-7, -3]$-meter interval due to the fast ripple of Surf. 1 field, see Fig. 8(b).

Fig. 8(b) shows that the received field due to surface 2 varies due to surface 1 blockage. Firstly, we observe a considerable magnitude drop at the middle of the interval due to surface 1 blockage of the direct component from the Tx antenna to surface 2. Secondly, a small ripple in surface 2 contribution is observed in the rest of the interval due to the virtually negligible effect of the blockage of surface 1. In the case of the field received due to surface 1, we observe a fluctuating magnitude increase as surface 1 moves toward the specular reflection point at the end of the interval ($x = 0$ m). Furthermore, Fig. 8(c) shows that when surface 1 centroid is near the end of the interval, surfaces 1 and 2 are out of phase and thus destructive interference is observed in Fig. 8(b). Lastly, even though the LoS component from Tx to Rx antenna is considered in the scenario, its impact is minor due to the pointing directions of the antennas.

IV. MEASUREMENT RESULTS

In order to further demonstrate the validity of the proposed model, a performance comparison against measurement results is presented here. In this section, we first consider a pure backscattering scenario and, second, a scenario featuring a multiple-scattered blocked component and a third-order backscattered component.

Measurements of S_{21} are performed in the 141–148 GHz frequency range by means of a vector network analyzer (R&S ZVA67 with R&S Z170). The scatterers are all metallic objects: surface 1 is a 17.9×15.0-cm book stand, and surface 2 is a 30.0×18.5-cm metal plate. Furthermore, the vertically-polarized, that is, z-polarized, antennas used in the measurements and modeled for the simulations are 25-dBi and 10-dBi standard gain horns (A-Info LB-6-25 and A-Info LB-6-10, respectively).

Note that, in the following, the model is used even when the ray optical continuation is not strictly valid, that is, when a specular reflection point falls outside the corresponding scattering surface or when blockage is present. The intervals where the ray optical continuation is strictly valid have been delimited by white dashed lines in the time domain results shown in this section.

A. First- and Second-Order Backscattering

Scenario E is designed such that, depending on surface 1 orientation, non-negligible first-order or second-order components will be measured. Specifically, the second-order component corresponds to the field travelling from the Tx antenna to the Rx antenna via the surfaces in inverse numerical order, see Fig. 9. Furthermore, the antennas are pointed such that the second-order component dominates, that is, the Tx and Rx antennas are pointed toward the specular reflection points in the planes defined by surface 1 and surface 2, respectively,
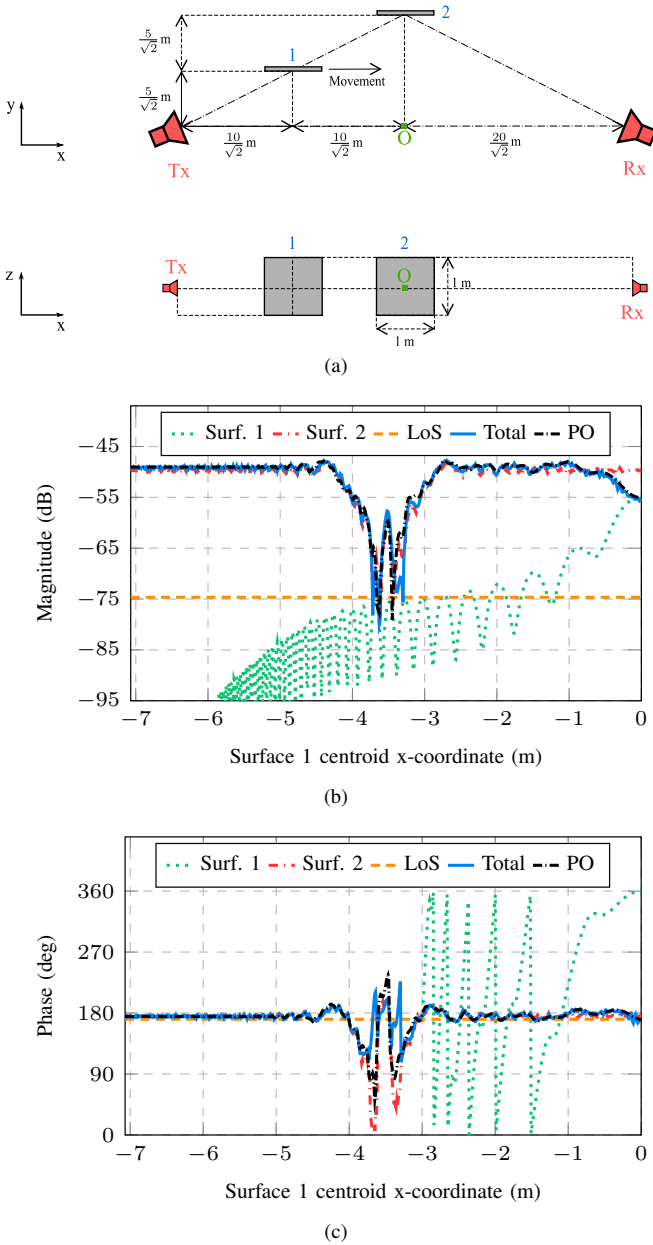
(a)

(b)

Fig. 8. Scenario D: Test-case with a moving "blocking" surface and a static surface. (a) From top to bottom: top projection and side-projection, respectively, of the middle-of-the-interval position of the blocking surface. (b) magnitude and (c) phase results of the 3D Fresnel and PO models for different displacements of the blocker.

(c)

when surface 1 has 45 degree rotation. For this purpose, surface 1 is rotated around its *z*-axis in the [0, 64]-degree interval, with zero denoting when surface 1 is parallel to the line connecting the Tx and Rx antennas and P_R denoting the origin of surface 1 local coordinate system. In this way, surface 1 has negligible impact at the beginning of the interval; adds first-order specular reflection near the middle of the interval; and finally adds second-order specular reflection via surfaces 1 and 2 near the end of the interval. This scenario was measured with a 5-MHz resolution, and with A-Info LB-6-10 and A-Info LB-6-25 used at Tx and Rx, respectively.

Fig. 10 displays scenario E results. First, Figs. 10(a)
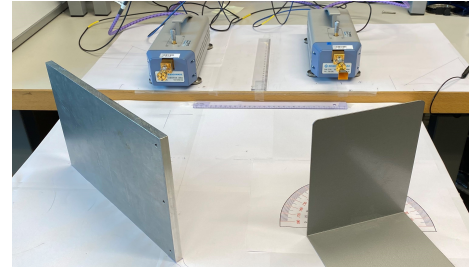
(a)
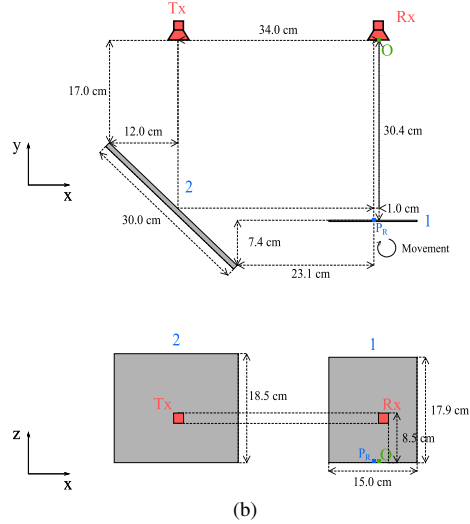
(b)

Fig. 9. Scenario E (a) lab set up picture and (b) (top) top projection and (bottom) side projection for the initial orientation of surface 1.

and 10(b) show frequency domain measured and 3D Fresnel model results, respectively. Apart from the good agreement of the 3D Fresnel model with the measured S_{21} results in the fundamental behavior, we observe a ripple in the measured results likely due to scattering in the measurement setup (or environment) that was not accounted for in the model. Second, Figs. 10(c) and 10(d) show the measured and 3D Fresnel model results in the time domain, respectively, calculated using the inverse Fourier transform with a Hann window. Two distinct components are clearly identified in the time domain: the previously introduced first- and second-order component, with the latter being stronger due to the antenna pointing. Due to the pointing of the antennas, the surface 2 single-scattering contribution is barely noticeable. In addition, to aid understanding, colored dashed lines have been added to indicate the geometrical distances of the different components traveling from antenna to antenna either directly or via the closest point to the corresponding specular reflection point in each surface. Hence, constant delay lines are obtained for static objects while variable delay is exhibited by the two components that depend on surface 1. Once more, good agreement between model and measurements is observed in the time domain.
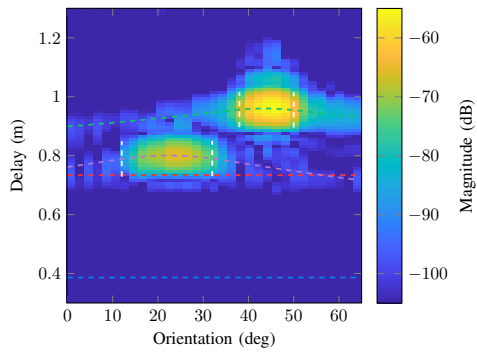
B. Third-Order Backscattering and First-Order Blockage

In scenario F, the surfaces are placed such that surface 1 blocks the illumination of surface 2 during surface 1
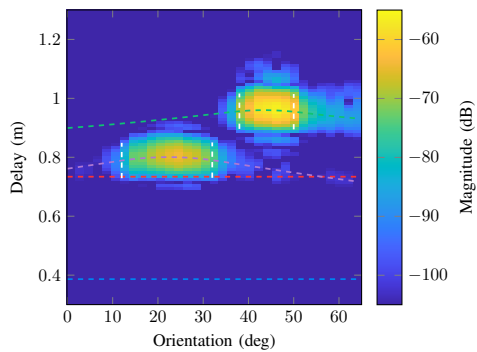
(a)

(b)
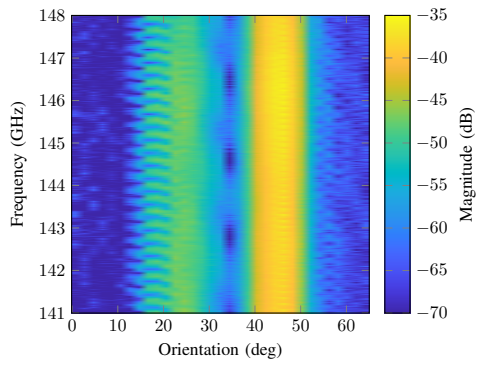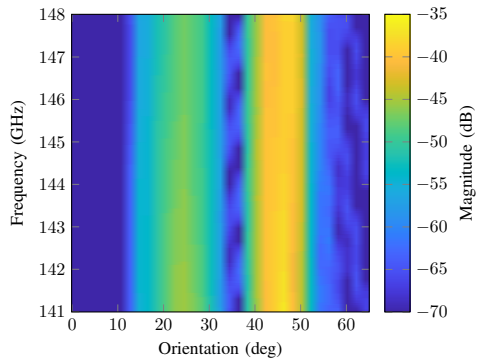
Fig. 10. Scenario E frequency domain (a) measured and (b) 3D Fresnel model results, and (c) measured and (d) 3D Fresnel model results in the time domain. Blue, purple, red, and green dashed lines indicate geometrical distances of the direct, surface 1 first-order, surface 2 first-order, and second-order components, respectively. White dashed lines indicate intervals where specular reflection points are contained within the surfaces.
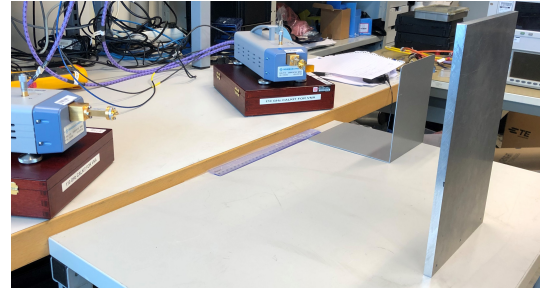

(a)
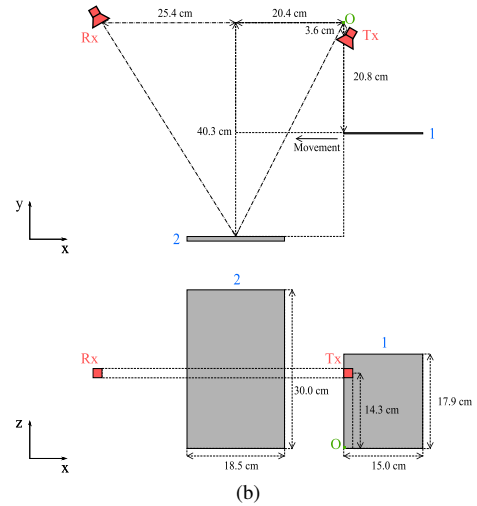
(b)

Fig. 11. Scenario F (c) lab set up picture and (d) (top) top projection and (bottom) side projection for the starting position of surface 1.

movement, see Fig. 11. For this purpose, surface 1 is moved along the *x*-axis in the $[0, -33]$-cm interval, with zero denoting the starting position. In this manner, surface 1 has negligible impact at the beginning of the interval; blocks the illumination of surface 2 near the middle of the interval; and finally adds first-order and third-order specular reflections at the end of the interval. This scenario was measured with a 10-MHz resolution, and with the antennas A-Info LB-6-25 and A-Info LB-6-10 used at Tx and Rx, respectively, both antennas pointing toward the specular reflection point in surface 2.

Figs. 12(a) and 12(b) display frequency domain measured S_{21} and 3D Fresnel model results, respectively, where very good agreement of the 3D Fresnel model with the measured results is again observed. The high variability in scenario F frequency domain results points to a smaller power difference among the components present in the scenario, which the time domain results confirm. Figs. 12(c) and 12(d) show the measured and 3D Fresnel model results in the time domain, respectively, again calculated using the inverse Fourier transform with a Hann window. Likewise, colored dashed lines have been added for indicating the geometrical distances of the different components. Again, very good agreement is achieved.
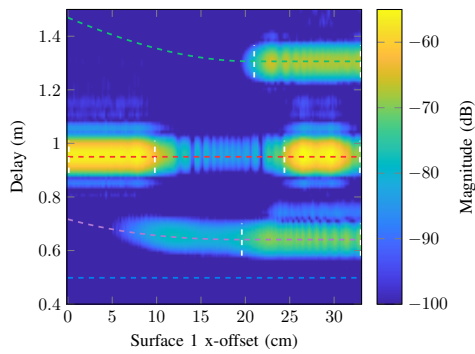
The time domain results in Figs. 12(c) and 12(d) feature several components. The LoS component, with a fixed delay of 0.50 meters, is weak due to the pointing of the antennas. Oppositely, and for the same reason (the antenna pointing), the component due to surface 2, with a fixed delay of 0.95
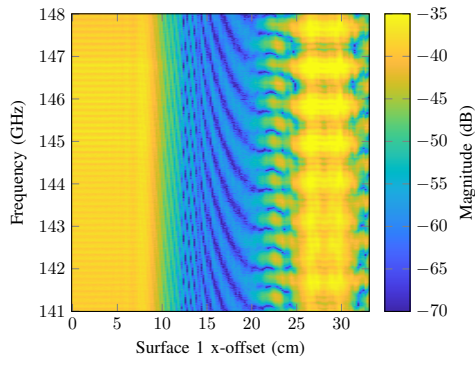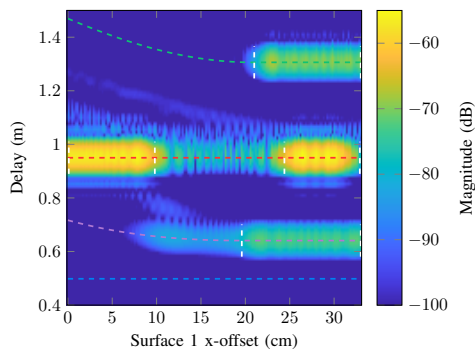
(a)
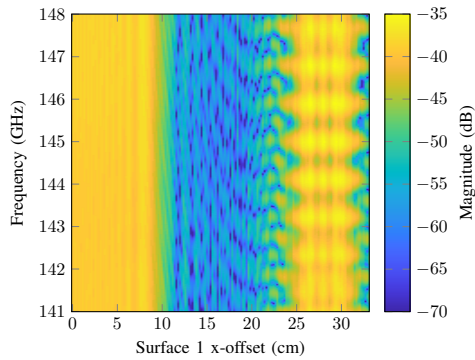
(b)

(c)

(d)

Fig. 12. Scenario F frequency domain (a) measured and (b) 3D Fresnel model results, and (c) measured and (d) 3D Fresnel model results in the time domain. Blue, purple, red, and green dashed lines indicate geometrical distances of the direct, surface 1 first-order, surface 2 first-order, and third-order components, respectively. White dashed lines indicate either intervals where specular reflection points are contained within the surfaces or, in the case of the surface 2 (delay marked in red), the interval where the specular reflection point is visible in surface 2, that is, not blocked by surface 1.
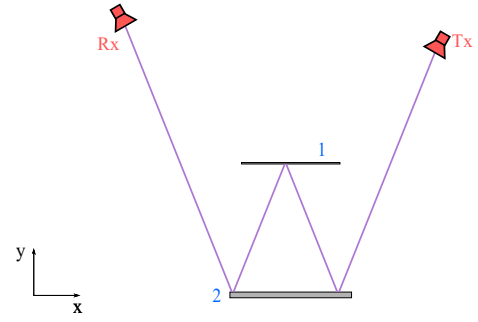

Fig. 13. Schematic drawing of the third-order component in scenario F for an example surface 1 x-offset of 27 cm.
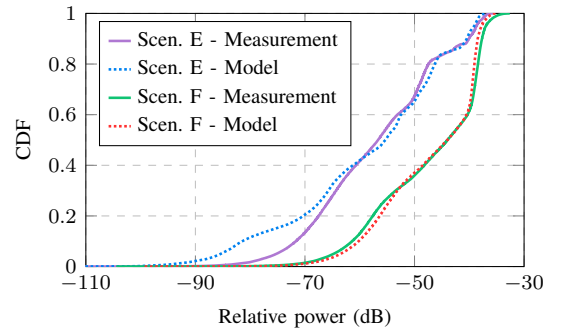

Fig. 14. Empirical CDFs of relative received power in the frequency domain for scenarios E and F.

meters, is the strongest in the scenario, except during the part of the movement interval where surface 1 is blocking the illumination of surface 2. The remaining two components show variable delay since they involve backscattering on surface 1, the moving surface. First, the single-scattering component on surface 1 shows a curved behavior (delay going from 0.71 to 0.64 meters) as the closest edge approaches the specular reflection. Once it is contained within the surface, the delay becomes constant. Finally, one last component comes into play due to further interactions: a third-order reflection following the Tx antenna, surface 2, surface 1, surface 2, and Rx antenna path. This third-order component presents variable delay between 1.47 and 1.30 meters for the same reason as explained in the case of surface 1 single-scattering component. The component has been indicated with a green line in Fig.13 to facilitate the understanding. Finally, the reason why the two latter components are weaker than the single-scattering component via surface 2 is, again, the antenna pointing.

Finally, Fig. 14 shows empirical cumulative distribution functions (CDFs) of scenarios E and F measured and model frequency domain results in Figs. 10(a), 10(b), 12(a), and 12(b). Good agreement is observed between measurements and model, especially in scenario F, with somewhat higher measured power in scenario E. The latter is likely due to an unmodeled weak scattering component in the measurement setup with larger delay than those that can be attributed to the test objects, as can be observed in the frequency domain results in Figs. 10(a) and 10(b). In conclusion, these measurement results support the validity of the proposed multiple-scattering